Resolving the Complexity of Spatial Lipidomics Using MALDI TIMS Imaging Mass Spectrometry

Djambazova, Katerina V.; Klein, Dustin R.; Migas, Lukasz G.; Neumann, Elizabeth K.; Rivera, Emilio S.; Van De Plas, Raf; Caprioli, Richard M.; Spraggins, Jeffrey M.

DOI
10.1021/acs.analchem.0c02520

Publication date
2020

Document Version
Final published version

Published in
Analytical Chemistry

Citation (APA)
Djambazova, K. V., Klein, D. R., Migas, L. G., Neumann, E. K., Rivera, E. S., Van De Plas, R., Caprioli, R. M., & Spraggins, J. M. (2020). Resolving the Complexity of Spatial Lipidomics Using MALDI TIMS Imaging Mass Spectrometry. *Analytical Chemistry*, *92*(19), 13290-13297. https://doi.org/10.1021/acs.analchem.0c02520

analytical chemistry

pubs.acs.org/ac Article

Resolving the Complexity of Spatial Lipidomics Using MALDI TIMS Imaging Mass Spectrometry

Katerina V. Djambazova, Dustin R. Klein, Lukasz G. Migas, Elizabeth K. Neumann, Emilio S. Rivera, Raf Van de Plas, Richard M. Caprioli, and Jeffrey M. Spraggins*

Cite This: *Anal. Chem.* 2020, 92, 13290−13297 Read Online

ACCESS | Metrics & More | Article Recommendations | Supporting Information

ABSTRACT: Lipids are a structurally diverse class of molecules with important biological functions including cellular signaling and energy storage. Matrix-assisted laser desorption/ionization (MALDI) imaging mass spectrometry (IMS) allows for direct mapping of biomolecules in tissues. Fully characterizing the structural diversity of lipids remains a challenge due to the presence of isobaric and isomeric species, which greatly complicates data interpretation when only m/z information is available. Integrating ion mobility separations aids in deconvoluting these complex mixtures and addressing the challenges of lipid IMS. Here, we demonstrate that a MALDI quadrupole time-of-flight (Q-TOF) mass spectrometer with trapped ion mobility spectrometry (TIMS) enables a >250% increase in the peak capacity during IMS experiments. MALDI TIMS-MS separation of lipid isomer standards, including *sn* backbone isomers, acyl chain isomers, and double-bond position and stereoisomers, is demonstrated. As a proof of concept, *in situ* separation and imaging of lipid isomers with distinct spatial distributions were performed using tissue sections from a whole-body mouse pup.

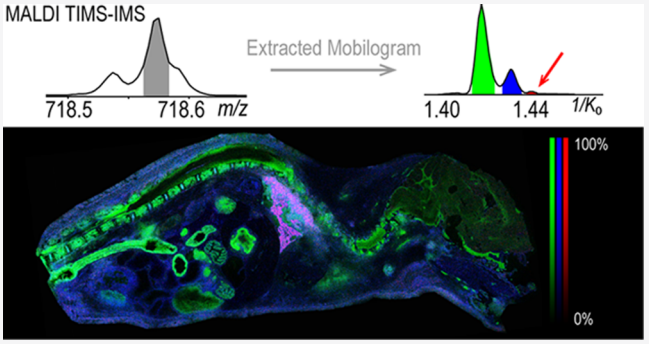

Lipids are crucial components of cellular membranes with essential functions in cellular structure, signaling, energy storage, and homeostasis.[1−4] They are structurally diverse molecules, with many having the same nominal mass and some having the same exact mass. Developing more comprehensive ways of characterizing these complex mixtures in tissues is important, as even subtle structural differences can have significant biological implications. Mass spectrometry (MS) is a powerful tool for lipid analysis with common *ex vivo* approaches utilizing electrospray ionization (ESI) and either direct infusion of lipid extracts or separations via liquid chromatography, neither of which retains spatial information of analytes in tissues.[3,5] In contrast, imaging mass spectrometry (IMS), which analyzes biomolecules *in situ*, enables highly specific mass analysis while retaining analyte spatial information.[6] Matrix-assisted laser desorption/ionization (MALDI), one of the most commonly used ionization techniques for IMS, permits visualization of lipids,[7,8] metabolites,[9,10] glycans,[11,12] peptides,[13,14] and proteins.[15,16] In a typical MALDI IMS experiment, tissues are thinly sectioned, mounted on a conductive glass slide, and coated with an ultraviolet-absorbing matrix. Desorption and ionization is facilitated by laser ablation at specific positions on the tissue surface. An individual mass spectrum is generated at each position (pixel), and molecular images are generated by plotting the ion intensity as a heat map across all of the pixels sampled on the tissue.[16] The spatial resolution of these chemical images is defined by the laser ablation area on the tissue and the spacing between the pixels (pitch).

The structural diversity of lipids in tissues can often be under-represented during MALDI IMS experiments owing to the presence of isobars and isomers that cannot be distinguished by their measured m/z alone. High resolving power and high mass accuracy instrumentation, including Fourier transform ion cyclotron resonance (FT-ICR) and Orbitrap mass analyzers, have been critical in enabling both lipid identification at the sum composition level, as defined by Liebisch et al.[2] and isobar differentiation.[17,18] However, structural isomers with identical masses cannot be separated simply by high mass resolving power instruments. In these cases, ion images of single m/z values may depict composites of multiple lipid species. Tandem MS (MS^n) has been used to reveal distributions of isomeric lipids *in situ*. Novel MS^n techniques, including low-energy collision-induced dissociation[19] with Paternò−Büchi derivatization,[20] ozone-induced dissociation,[21] and ultraviolet photodissociation,[22] have

Received: June 13, 2020
Accepted: August 18, 2020
Published: August 18, 2020

https://dx.doi.org/10.1021/acs.analchem.0c02520
Anal. Chem. 2020, 92, 13290−13297

revealed differential localization of double-bond positional and *sn* positional isomers. While MS^n techniques provide a higher degree of structural characterization, they are highly targeted.[23] Integration of online chromatographic separation with direct tissue sampling can increase the specificity of an IMS experiment, however, this setup typically requires lengthy acquisition times.[24,25] Alternatively, chromatographic techniques can be applied to serial tissue sections to further increase the specificity of an IMS experiment.

Ion mobility enables gas-phase separation of molecules according to their shape, size, and charge on timescales (microsecond to millisecond) that are compatible with typical IMS experiments. Ion mobility separation techniques include drift tube ion mobility spectrometry (DTIMS),[26,27] traveling wave ion mobility spectrometry (TWIMS),[28,29] field asymmetric ion mobility spectrometry (FAIMS),[30−32] and trapped ion mobility spectrometry (TIMS).[33,34] DTIMS and TWIMS are operated under lower-pressure regimes and have typically been coupled to time-of-flight (TOF) mass spectrometers. Mobility trendlines generated during DTIMS and TWIMS experiments have been beneficial for identifying classes and subclasses of lipids and have also enabled increases in signal-to-noise.[27,28] DTIMS and TWIMS have both been used to separate ESI-generated lipid isomers, including *sn* positional, double-bond positional, and stereochemical isomers (R versus S).[35−37] Furthermore, both TWIMS and DTIMS have previously been utilized on instruments capable of imaging mass spectrometry.[38,39] Recent developments in TWIMS technologies have led to the development of structures for lossless ion manipulations (SLIM)[40−43] capable of high-resolution separations of many lipid isomers.[38] Although SLIM shows promise for elucidating subtle structural differences, it has only been coupled to liquid surface probes and has not yet been integrated with a MALDI IMS setup.[45] FAIMS devices do not require low pressures and can be integrated in a variety of mass spectrometers.[46] With the exception of a higher-resolution planar-FAIMS device,[44] most FAIMS devices operate at relatively low resolving power and are used to filter specific classes or subclasses of lipids.[36] For example, shotgun lipidomic studies with FAIMS have been successful in lipid class separations,[36,47] and Lintonen et al. have shown the use of FAIMS for the construction of lipid class trendlines.[48] Similar to DTIMS and TWIMS, FAIMS has also been coupled to IMS platforms. For example, Feider et al. have demonstrated improved detection and imaging of cardiolipins in rat brain with the use of FAIMS and desorption electrospray ionization.[49]

Recently, TIMS integration with IMS has shown great potential for high-resolution separations.[50] TIMS platforms are capable of resolving powers >200 in 50−500 ms.[34,51−53] Briefly, TIMS is performed in the first vacuum stage of the mass spectrometer in an augmented ion funnel. An electric field gradient (EFG) is applied to the ion tunnel to trap ions against a carrier gas and separate them based on mobility. Following ion trapping, the EFG is gradually reduced to sequentially elute ions with ascending mobilities.[33,52] The voltage range (ΔV_{ramp}) and ramp time (t_{ramp}) dictate the scan rate ($S_r = \Delta V_{ramp}/t_{ramp}$),[54] with slower scan rates resulting in higher-resolution separations. While a MALDI TIMS-MS platform has successfully been used to separate and spatially map lipid species that overlap in m/z space, a full assessment of the effect of TIMS on peak capacity and isomer separation in an imaging context has not yet been demonstrated.[50,55] In addition, the ability of TIMS to resolve isomeric lipids via liquid chromatography-TIMS-MS suggests that it has the capability to resolve isomeric lipids *in situ*.[50]

Here, we present the use of the TIMS technology for increased peak capacity and deconvolution of complex lipid mixtures in an imaging context. The high-resolution separation of the MALDI-generated lipid isomer standards is demonstrated, followed by an *in situ* assessment of lipid peak capacity using TIMS-IMS and visualization of the lipid isomers in a full-body mouse pup tissue. These data provide the foundation for maximizing the sensitivity and specificity of lipid imaging experiments on TIMS-based MALDI platforms.

METHODS

Materials. 1,5-Diaminonaphthalene (DAN) and 2′,5′-dihydroxyacetophenone (DHA) were purchased from Sigma-Aldrich (St. Louis, MO). High-performance liquid chromatography (HPLC)-grade acetonitrile, methanol, ethanol, chloroform, and tetrahydrofuran (THF) were purchased from Fisher Scientific (Pittsburgh, PA). Lipid standards were purchased from Avanti Polar Lipids (Alabaster, AL).

Sample Preparation. For tissue preparation, 1 week old C57BL/6 control mouse pup was snap-frozen at −80 °C, shaved over dry ice, and cryosectioned (20 μm thickness), using a CM3050 S cryostat (Leica Biosystems, Wetzlar, Germany). The tissue was thaw-mounted onto conductive indium tin oxide-coated glass slides (Delta Technologies, Loveland, CO). The sample was placed on a heated metal block (75 °C) and coated with a 15 mg/mL solution of DAN dissolved in THF using a TM Sprayer (HTX Technologies, LLC, Chapel Hill, NC) (0.05 mL/h, 5 passes, 0 s drying time, 40 °C spray nozzle). For lipid standard analysis, the standards (in chloroform) were aliquoted in vials (5 mg/mL), dried down with nitrogen gas, and dissolved in 80% methanol for a final concentration of 1.0 mg/mL. The aliquots were then mixed with DHA matrix, dissolved in 90% acetonitrile for a final lipid concentration of 0.2 mg/mL. The mixtures were spotted on a polished steel target—MTP AnchorChip (Bruker Daltonik, Bremen, Germany).

MALDI TIMS-IMS. All experiments were carried out on a prototype timsTOF fleX mass spectrometer (Bruker Daltonik, Bremen, Germany).[50] Images were acquired in TIMS mode of operation with an ion transfer time of 100 μs, prepulse storage time of 8 μs, and a collision RF of 2000 Vpp, a TIMS funnel 1 (accumulation) RF of 450 Vpp, a TIMS funnel 2 RF (analysis) of 400 Vpp, a multipole RF of 400 Vpp, and a collision cell entrance (in) voltage of 300 V. Tissue imaging data (1 96 514 pixels) were collected at 50 μm spatial resolution with beam scan on (46 μm), using 200 shots per pixel and 48% laser power. Data were collected in positive ionization mode from m/z 50 to 1500. The TIMS EFG scan time was set to 650 ms, with reduced a mobility ($1/K_0$) range of 1.370−1.520 (V·s)/cm^2 (S_r = 0.03 V/ms). TIMS imaging data was visualized using custom in-house developed software. Lipid identifications were determined with high mass accuracy and LIPIDMAPS lipidomics gateway (lipidmaps.org[56,57]).

Lipid standards data were acquired in TIMS mode of operation with the specific tuning of TIMS ramp time, mobility range, and scan rate for each of the analyzed standards. Data were acquired at 20 μm spatial resolution with ∼25% laser power at 10 kHz, 200 shots per pixel, and ∼200 pixels per sample. Based on the laser repetition rate and the number of shots per pixel, the ion accumulation time per pixel was 20 ms.

https://dx.doi.org/10.1021/acs.analchem.0c02520
Anal. Chem. 2020, 92, 13290−13297

For all isomer standard experiments, the ramp time (t_{ramp}) was kept constant (650 ms), and the mobility range was manipulated such that the voltage change (ΔV_{ramp}) and therefore scan rate (S_r = ~0.01 V/ms) were kept constant across all experiments. A full list of the experimental parameters is included in Table S1.

MALDI FT-ICR IMS. Whole-body mouse pup tissue data were acquired using a 15T MALDI FT-ICR mass spectrometer (Bruker Daltonics, Billerica, MA). The images were generated with the "small" laser setting of ~50 μm, with a spatial resolution of 150 μm. The data was collected with 300 laser shots per pixels at 46% laser power. The recorded mass spectrum had a m/z range of 460−1500 with a transient length of 4.2 s, resulting in a resolving power of ~600 000 at m/z 760.

Data Processing. The mouse pup data was exported into a custom binary format optimized for storage and speed of analysis of the ion mobility-IMS data collection. Each frame/pixel contains between 10 000 and 1 00 000 centroid peaks that span the acquisition range of m/z 50−1500 and $1/K_0$ 1.370−1.520 (V s)/cm^2 with 400 577 and 5857 bins in the MS and ion mobility dimensions, respectively. The processing pipeline requires common m/z and $1/K_0$ axes, hence individual centroid peaks were inserted at their correct bin position along the MS and ion mobility dimensions; missing values were set to zero. Following the conversion process, a mean mass spectrum of the entire data set was generated and peak-picked. A total of ~400 most intense ions were then selected and extracted to generate ion mobility-rich ion images. Each of the extracted ion mobility-ion images was peak-picked (in the ion mobility dimension) and automatically fitted with Gaussian distributions to identify single and multiconformational species. Ion mobility-selected ion images were then visualized to examine the conformational-specific localization in the spatial domain.

Peak capacity refers to the number of detectable features. A peak in the m/z domain corresponds to a spectral feature for which the area under the curve (AUC) was calculated and the full-width at half-maximum (FWHM) was determined. An in-house developed peak picker was used to create a list of spectral features found in the average mass spectrum, which were then filtered based on the minimal intensity (>0.1% of the base peak). In the TIMS dimension, a peak corresponds to a feature that was fitted with a single Gaussian curve allowing for the calculation of the AUC and FWHM. Ion mobility profiles containing multiple conformations were fitted with multiple Gaussian peaks to represent the profile, as a single m/z species can have several IM features.

RESULTS AND DISCUSSION

TIMS Peak Capacity. Direct sampling of lipids from the tissues by imaging mass spectrometry produces complex mass spectra. To assess the advantage of incorporating TIMS into an IMS workflow, spectral peak capacity (i.e., the number of detectable features) was determined for an average spectrum of a whole-body mouse pup tissue image. Peak capacity is determined by peak picking the data to identify the number of unique mass spectral features with and without incorporating TIMS data. When the TIMS dimension is incorporated, the peak capacity is determined as the number of unique mass spectral and associated mobility features. The average mass spectrum from m/z 680 to 880 with no ion mobility separation shown in Figure 1A has a peak capacity of 247. Over the same m/z range, with a 650 ms TIMS separation, the peak capacity increases to 916. Figure 1B provides a heat map representation of the ion mobility-MS data. Integrating ion mobility into the MALDI IMS workflow, therefore, provides a >250% increase in the number of species detected for lipid IMS experiments.

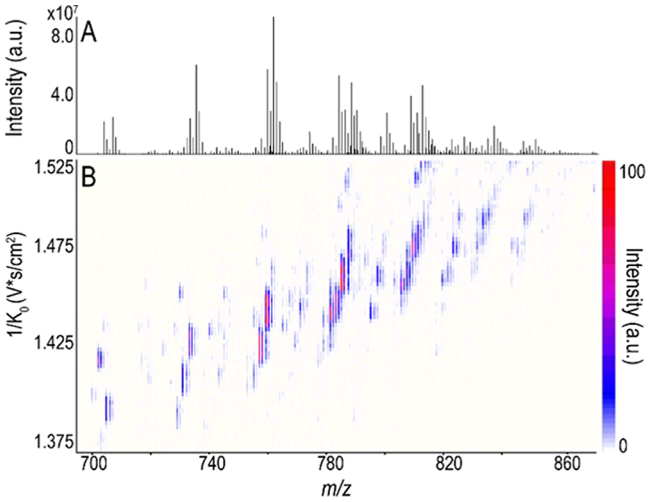

Figure 1. Average mass spectrum (A) and ion mobility heat map (B) generated for average whole-body mouse pup data highlight the presence of multiple isobaric and isomeric species. The diversity of ions observed in the heat map for each m/z highlight the complexity of the data and demonstrate the increased peak capacity by incorporating the TIMS separation dimension. The mass spectrum ranges include m/z values 680−880 and the heat map incorporates $1/K_0$ values 1.375−1.500.

The increased peak capacity afforded by the TIMS results from the separation of isobaric and isomeric species that otherwise overlap in the m/z dimension. A well-documented example of isobaric interference that occurs with lipid analysis results from overlap of an M + 2 isotopologue of one species with the monoisotopic (M) peak of another lipid with one less double bond. This "double-bond ambiguity" gives rise to a mass difference of 0.00895 Da.[58] Peak overlap that results from unresolved isotopic distributions can lead to artificially high mass errors that preclude lipid identification.[58,59] While TOF instruments generally are not able to resolve peaks resulting from lipid double-bond ambiguity, the added dimension of ion mobility allows for gas-phase separations that help address this spectral complexity. Figure 2 provides an example of how TIMS can resolve overlapping isotopes for the ion of m/z 848.55. With a mobility separation time of 650 ms, the ion of m/z 848.55 resolves into two mobility peaks at $1/K_0$ 1.485−1.499 and $1/K_0$ 1.468−1.485. Figure 2A shows the composite ion image combining the mobility-separated species for m/z 848.55. Figure 2B,C shows the individual ion images for $1/K_0$ 1.485−1.499 and $1/K_0$ 1.468−1.485, respectively, each of which localizes to distinct regions of the tissue. For example, $1/K_0$ 1.485−1.499 is found at higher abundance in the brain and with more distinct localization to the intestinal walls as compared to $1/K_0$ 1.468−1.485, which shows unique localization in the adipose tissue. Figure 2D shows the ion image of m/z 846.54 for the mobility range of $1/K_0$ 1.468−1.485, which, by comparison, localizes to the same regions of tissues as m/z 848.55 for the mobility range of $1/K_0$ 1.468−1.485. Considering the intact mass measurements and differences in spatial localizations, the species at m/z 848.55 with a mobility elution time of 1.485−1.499 likely corresponds to the monoisotopic peak of phosphatidylcholine (PC) [PC(38:4)

https://dx.doi.org/10.1021/acs.analchem.0c02520
Anal. Chem. 2020, 92, 13290−13297

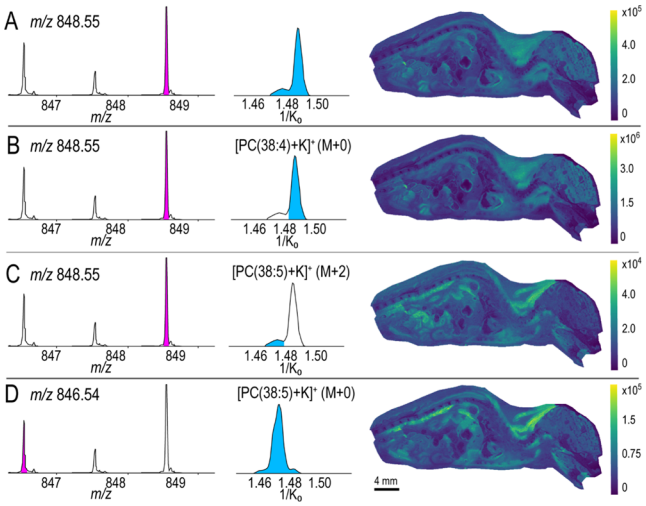

Figure 2. Added dimension of ion mobility helps address spectral ambiguities to show how the double-bond ambiguity is resolved for the ion of m/z 848.55. The ion of m/z 848.55 resolves into two peaks at $1/K_0$ 1.485−1.499 and $1/K_0$ 1.468−1.485 (A). Composite image of the two peaks (A) and individual ion images for $1/K_0$ 1.485−1.499 (B) and $1/K_0$ 1.4768−1.485 (C) highlight differences in their spatial distributions. The ion image of m/z 846.54 ($1/K_0$ 1.468−1.485) (D) localizes to the same regions as m/z 868.55 for the mobility range of $1/K_0$ 1.468−1.485 (C). Species of m/z 848.55 with $1/K_0$ 1.485−1.499 likely corresponds to the M + 0 (monoisotopic) peak of $[PC(38:4) + K]^+$, while the species of m/z 848.55 with $1/K_0$ 1.468−1.485 corresponds to the M + 2 peak of $[PC(38:5) + K]^+$.

$+ K]^+$, while the species of m/z 848.55 with a mobility elution time of 1.468−1.485 corresponds to the M + 2 peak of $[PC(38:5) + K]^+$. Without a mobility separation, m/z 848.55 would likely be assigned solely as the higher-intensity $[PC(38:4) + K]^+$ and the generated ion image would provide a skewed representation of its distribution throughout the tissue.

Separation of MALDI-Generated Lipid Isomer Standards. The isomers have the same chemical formulas (identical m/z values) and therefore cannot be separated in m/z space. Gas-phase separations prior to MS analysis have been successful in resolving isomeric species. Here, MALDI TIMS isomer separations were evaluated in both positive and negative ion mode. The performance was assessed using standards including isomers with differences in *sn* position, acyl chain composition, double-bond position, and double-bond stereochemistry (Figure S1). These standards have previously been characterized using ESI techniques in combination with TIMS, as well as other separation techniques.[37,60] MALDI TIMS analyses, however, lay the groundwork for isomer differentiation within a molecular imaging context. The mass spectra of the individual standards can be found in Figures S2 and S3. Extracted ion mobilograms were generated for each standard as well as for the mixtures of isomeric standards. Both ion mobility resolving power (R) and resolution (r) defined as $R = (1/K_0)/w$ and $r = 1.18 \times (1/K_{0,2} - 1/K_{0,1})/(w_1 + w_2)$, where w is the full peak at half-maximum, were calculated.

***sn*-Position.** Subtle differences in glycerophospholipid structure, including differences in acyl chain positions, can have dramatic effects on biological functions. A unique case of the *sn* positional isomers is bis(monoacylglycerol)phosphates (BMPs) and phosphatidylglycerols (PGs). In contrast to PGs, where both acyl chains are connected to the glycerol backbone, BMPs have one acyl chain connected at the *sn*-1 position on the glycerol backbone and a second acyl chain connected to the *sn*-1′ position of the glycerol headgroup, resulting in an unusual *sn*-1:*sn*-1′ orientation.[37,61] Differentiation of BMPs and PGs is important, as both are present in mammalian cells, but differ in their biological roles and cell locations. BMP lipids have been found in the endosomal and lysosomal compartments of the cell and have been associated with the Niemann−Pick disease, an endosomal/lysosomal storage disease.[62,63] PGs, on the other hand, are thought to have antiviral properties, inhibiting viral proliferation in the lungs including respiratory syncytial virus.[61,64]

sn positional isomers are particularly challenging to characterize as collision-based tandem mass spectrometry methods produce spectra with only differences in ion abundances, i.e, nonunique identifying ions.[61] To evaluate MALDI TIMS as a platform to separate PG and BMP isomers, mobility data was collected for the standards PG (14:0/14:0) and BMP (14:0/14:0) (Figure 3A). Standards were first analyzed individually to determine mobility values. The MS1 spectrum for each standard contains a predominant ion of m/z 665.49, corresponding to the $[M - H]^-$ species for each lipid. The measured $1/K_0$ values were 1.268 and 1.283 for PG (14:0/14:0) and BMP (14:0/14:0), respectively. The difference in backbone orientation results in an increased distance between the acyl chains and consequently an increased difference in collision cross section between BMP and PG.[37] A 1:1 mixture was analyzed to evaluate the separation of the isomers. An extracted ion mobilogram was generated for the deprotonated species (m/z 665.49), and the two peaks could be resolved in the mobilogram (1.270 and 1.282). The mobilogram of the mixture shows separation of the two species with a resolution of 0.84. Based on the $1/K_0$ values, our results indicate that the PG has a more compact structure than the BMP, which is consistent with previous studies.[37,61]

Acyl Chain Composition, Double-Bond Position, and Double-Bond Stereochemistry. The biophysical effects of acyl chain compositions and the positions and stereochemistry (cis (Z) vs trans (E)) of double bonds in lipid acyl chains are well-documented.[65,66] The thickness and fluidity of biological membranes are affected by lipid double-bond stereochemistry, as well as acyl chain length.[35,37] Specifically, shorter acyl chains and cis double bonds result in thinner, more fluidic membranes.[67] Lipids with trans double bonds are known to cause changes in membrane function and inhibition of lipid enzymatic pathways.[35] Differences in double-bond position, on the other hand, have been linked to the development of various diseases, including cancer and type-2 diabetes,[68] and have been known to influence lipid−protein binding.[69] To assess the separation capabilities of MALDI TIMS for the isomers in both negative and positive ionization mode, the lipids with differences in the acyl chain composition, double-bond position, double-bond stereochemistry, and combinations of composition, position, and stereochemistry were examined. First, MALDI TIMS was performed in negative ionization mode for the deprotonated ions of PG (18:1(9E)/18:1(9E)) and PG (18:0/18:2(9Z,12Z)) (Figure 3B). Both lipids have two unsaturations: PG (18:0/18:2(9Z,12Z)) has two double bonds on the same acyl chain in cis stereochemistry and PG (18:1/18:1(9E)) has a single unsaturation on each chain with trans stereochemistry; these lipid standards differ in acyl chain composition, double-bond position, and double-bond stereochemistry. The mass spectrum of each standard was dominated

https://dx.doi.org/10.1021/acs.analchem.0c02520
Anal. Chem. 2020, 92, 13290−13297

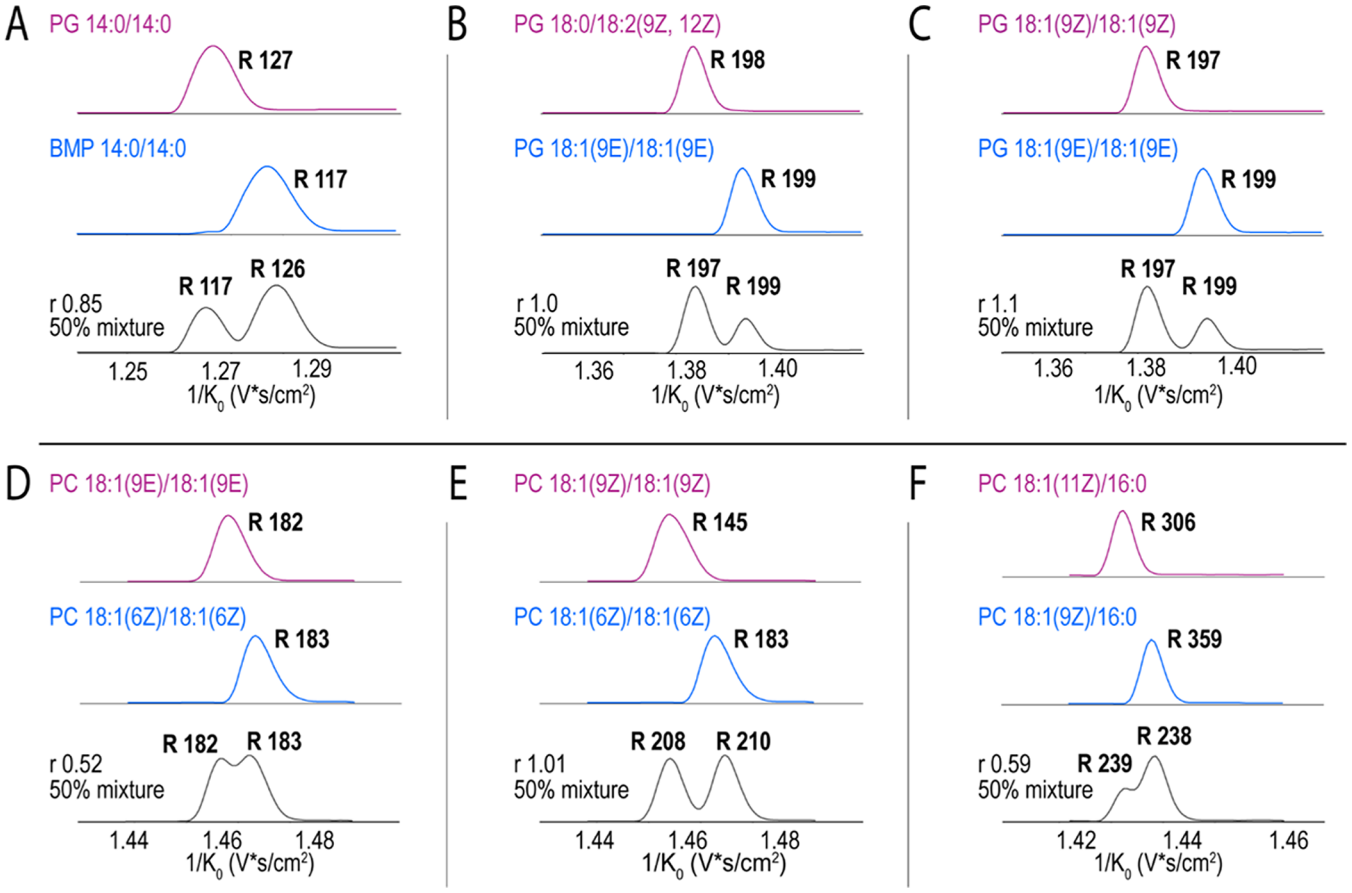

Figure 3. Extracted ion mobilograms of the MALDI-generated ions of the isomeric lipid standards are shown for both negative (A–C) and positive ionization mode (D–F). Negative ionization mode analysis of *sn* backbone isomers PG (14:0/14:0) and BMP (14:0/14:0) ($[M - H]^-$, m/z 665.49) (A); analysis of double-bond position and stereoisomers—G (18:0/18:2 (9Z, 12Z)) and PG (18:1/18:1 (9E)) (B) and PG (18:1(9Z)/18:1 (9Z)) and PG ((18:1(9E)/18:1(9E)) ($[M - H]^-$, m/z 773.53) (C). Positive ion mode analysis of double-bond position and stereoisomers—PC (18:1(9E)/18:1(9E)) and PC (18:1(6Z)/18:1(6Z)) (D) and PC (18:1(9Z)/18:1(9Z)) and PC(18:1(6Z)/18:1(6Z)) ($[M + Na]^+$, m/z 808.57) (E), as well as PC (18:1(11Z)/16:0) and PC18:1(9Z)/16:0) ($[M + Na]^+$, m/z 782.56) (F). Resolving power (R) is listed where appropriate.

by the $[M - H]^-$ ion at m/z 773.53. The measured $1/K_0$ values for PG (18:1(9E)/18:1(9E)) and PG (18:0/18:2-(9Z,12Z)) were 1.394 and 1.383, respectively. The lower $1/K_0$ value for PG (18:0/18:2(9Z,12Z)) suggests that it assumes a more compact gas-phase structure. A mixture of the two standards shows partial separation (r = 1.0), suggesting that the isomers with differences in acyl chain composition, double-bond position, and stereochemistry could be resolved *in situ*. To further test the separation capabilities for more subtle differences in structures, mobility data were collected for PG (18:1(9E)/18:1(9E)) and PG (18:1(9Z)/18:1(9Z)), where the only difference is double-bond stereochemistry. Extracted ion mobilograms of the deprotonated species (m/z 773.53) are shown in Figure 3C. The measured $1/K_0$ values for individual PG (18:1(9Z)/18:1(9Z)) and PG (18:1(9E)/18:1(9E)) are 1.381 and 1.394, respectively. The mixture of PG (18:1(9Z)/18:1(9Z)) and PG (18:1(9E)/18:1(9E)) confirms that the deprotonated species of each lipid can be well resolved (r = 1.1). Based on the lower mobility value, PG (18:1(9Z)/18:1(9Z)) takes on a more compact gas-phase structure than PG (18:1(9E)/18:1(9E)). Our results from both isomer pairs suggest that the lipids with cis double bonds have more compact structures than lipids with trans double bonds. These findings are aligned with the existing literature, as cis double bonds are believed to introduce a bend or curl in in otherwise linear acyl chains.[37]

MALDI TIMS separations of double-bond position and stereoisomers were also evaluated for cationic lipids. All positive ionization mode analysis was carried out on sodium-adducted PC standards. Figure 3D shows the extracted ion mobilograms of the $[M + Na]^+$ ion (m/z 808.57) for PC (18:1(6Z)/18:1(6Z)) and PC (18:1(9E)/18:1(9E)) that vary in both double-bond position and double-bond stereochemistry. The individual mobilograms of the sodiated species show that PC (18:1(9E)/18:1(9E)) ($1/K_0$ 1.462) has a lower mobility value than PC (18:1(6Z)/18:1(6Z)) ($1/K_0$ 1.468); the two standards are not well resolved from a mixture of the standards (r = 0.52). Our results suggest that the 9E isomer results in a more compact structure than the 6Z, which is consistent with previously published data, suggesting that the trans orientation is more impacted by the sodium adduct, pulling it closer to the headgroup, resulting in a more compact conformation than the 6Z.[54] To investigate the effect of double-bond position alone, standard PC (18:1(6Z)/18:1(6Z)) was analyzed with PC (18:1(9Z)/18:1(9Z)) (Figure 3E). The individual extracted ion mobilograms (m/z 808.57) show that the 9Z isomer results in a smaller structure than the 6Z, with $1/K_0$ 1.458 and 1.468, respectively. The

https://dx.doi.org/10.1021/acs.analchem.0c02520
Anal. Chem. 2020, 92, 13290−13297

mobilograms of the mixture show separation of the two species with a resolution of 1.01. Our results indicate that the 9Z results in a more compact structure. This finding is also supported by the previous literature, stating that cis double bonds further from the carboxyl end curl the acyl chain more, causing smaller conformations.[37] In addition to the aforementioned lipid isomers, PC (18:1(9E)/18:1(9E)) and PC (18:1(9Z)/18:1(9Z)) were analyzed to evaluate the separation of the isomers with cis vs trans stereochemistry (Figure S4).

Finally, mobility separations were performed on the $[M + Na]^+$ ion (m/z 782.56) of PC (18:1(9Z)/16:0) and PC (18:1(11Z)/16:0) (Figure 3F), the isomers that vary only in the position of a single double bond. These lipid species are generally abundant in biological tissues and represent an interesting biological target. For instance, Paine et al. have demonstrated that although both PC (18:1(9Z)/16:0) and PC (18:1(11Z)/16:0) are found in the rat brain tissue, their relative abundances vary between white matter and gray matter.[70] The individual mobilograms suggest that the 11Z ($1/K_0$ 1.430) isomer has a more compact structure than the 9Z (1.436). Despite the difference in a single double-bond location being very subtle, slight separation in the mobilogram was still observed (r = 0.59).

MALDI TIMS Separation and Localization of the Lipid Isomers in Whole-Body Mouse Pup Tissues. MALDI TIMS-IMS was used to visualize the spatial distribution of the lipid isomers in whole-body mouse pup tissues. From the average mass spectrum, an example of isomeric overlap is highlighted at m/z 718.58, where three distinct species are resolved in the extracted ion mobilogram (Figure 4A). A composite ion image for m/z 718.58 including all observed mobility peaks from $1/K_0$ 1.410 to 1.452 (Figure 4A) was generated, followed by ion images for each ion mobility-separated species (Figure 4B–D). Each ion has a unique spatial distribution within the mouse pup tissue. The ion with $1/K_0$ 1.410–1.428 (Figure 4B) is the highest-intensity ion that localizes to the organs of the abdominal cavity, the spinal cord, and the brain with lower intensity. The ion with $1/K_0$ 1.430–1.441 (Figure 4C) localizes primarily to the liver, to the connective tissue, and is completely absent in the brain. Finally, the ion with mobility $1/K_0$ 1.446–1.452 (Figure 4D) localizes to the liver and has very low intensity or is completely absent throughout the rest of the body. From the composite image, the highest-intensity ion ($1/K_0$ 1.410–1.441) dominates the ion image, and the spatial distributions of the other two ions are lost. An overlay image of each of the ion mobility-resolved species is shown in Figure 4E, highlighting the unique spatial distributions of each of these lipids. To determine if these ions were isobars or isomers, a serial section of the whole-body mouse pup was analyzed using ultrahigh-resolution FT-ICR MS (resolving power of ~600 000 at m/z 760). The whole-body average FT-ICR spectrum suggests that the ions separated in mobility space are, in fact, isomers (Figure S5). An ion image was generated for m/z 718.58, and the localizations match well to the MALDI TIMS composite ion image (Figure 4A). This data further confirms that the composite ion image of m/z 718.58 is biased toward the most intense ion in the mass spectrum (Figure S5). The FT-ICR MS data was also used to assist in identifying the ions (Figure S5). From the FT-ICR mass spectrum, there are no nominally interfering peaks and no overlapping isotopic distribution could be detected. Based on the mass accuracy alone, the three isomeric species were tentatively identified as $[CerP(t40:1) + H]^+$, $[PC(O\text{-}32:1) + H]^+$, and $[PC(P\text{-}32:0) + H]^+$ (0.14 ppm error). This example highlights the utility of coupling TIMS with MALDI IMS.

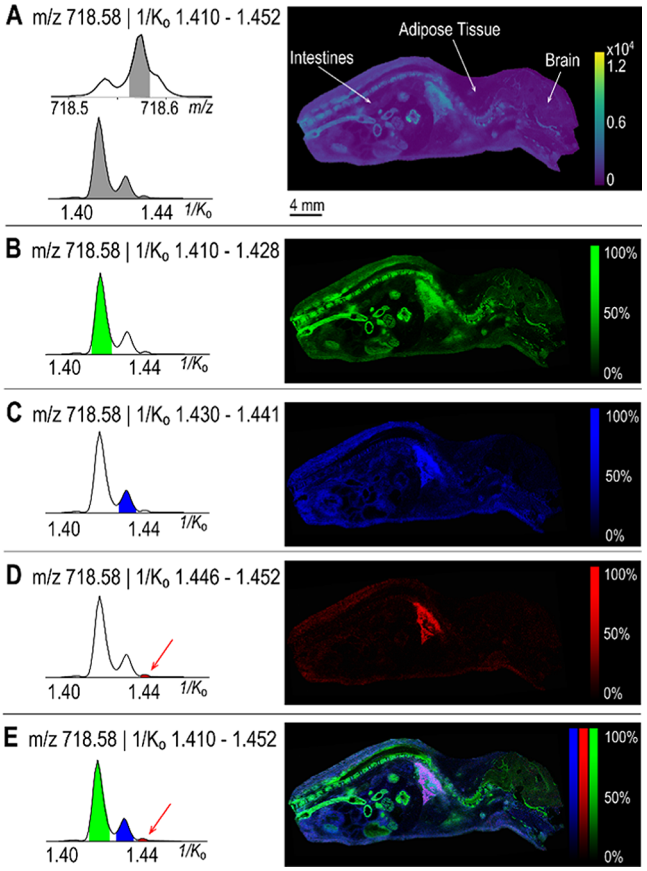

Figure 4. TIMS enables the separation of the lipid isomers in the whole-body mouse pup tissues. A composite image of all three peaks in the extracted ion mobilogram ($1/K_0$ 1.410–1.452) of m/z 718.58 is shown (A). Each panel highlights an ion image generated for three distinct mobility range, $1/K_0$ 1.410–1.428 (B), 1.430–1.441 (C), and 1.446–1.452 (D), and an overlay of all three mobility peaks (E). The three ions have different localizations across the tissue sample; however, the average ion image (A) is dominated by the spatial distributions of the highest-intensity ion (B). The ions were putatively identified as $[CerP(t40:1) + H]^+$, $[PC(O\text{-}32:1) + H]^+$, and $[PC(P\text{-}32:0) + H]^+$ (0.14 ppm error) based on accurate mass alone.

CONCLUSIONS

This work has demonstrated the use of a MALDI timsTOF IMS for enhanced peak capacity and lipid isomer analysis. An additional 669 features were detected by incorporating TIMS, resulting in a >250% increase in peak capacity. MALDI TIMS separation of the lipid isomer standards, including *sn* backbone isomers, acyl chain isomers, and double-bond position and stereoisomers, was also demonstrated. Of note is the partial separation of PC (18:1(9Z)/16:0) and PC (18:1(11Z)/16:0). The two species vary in a single double-bond location and require high resolving powers (>250) to separate in mixtures. Resolving these standards lays important groundwork for further MALDI TIMS-IMS experiments, as both species are generally abundant in biological tissues, but may differ in relative abundances.[70]

Finally, *in situ* separation and imaging of the lipid isomers with distinct spatial distributions was performed using whole-

https://dx.doi.org/10.1021/acs.analchem.0c02520
Anal. Chem. 2020, 92, 13290–13297

body mouse pup tissues. Gas-phase isobar and isomer separations confirm TIMS as a valuable tool that can bring new dimensions to IMS experiments. Lipid identification, however, remains a challenge, and TIMS data was supplemented with MALDI FT-ICR imaging to provide tentative lipid isomer identifications. Here, we show that incorporating TIMS in a MALDI IMS workflow enhances the specificity of the experiment. Building on this, future multimodal studies that combine high-performance MALDI TIMS with advanced structural identification methods has the potential to further increase the depth of characterization of the lipids *in situ*.

■ ASSOCIATED CONTENT

Supporting Information

The Supporting Information is available free of charge at https://pubs.acs.org/doi/10.1021/acs.analchem.0c02520.

Experimental TIMS parameters (Table S1); names, structures, and masses of the lipid standards (Figure S1); negative ionization mode mass spectra of standards (Figure S2); positive ionization mode mass spectra of standards (Figure S3); extracted ion mobilogram of PC (18:1(9Z)/18:1(9Z)) and PC (18:1(9E)/18:1(9E)) (Figure S4); MALDI FT-ICR data (Figure S5) (PDF)

■ AUTHOR INFORMATION

Corresponding Author

Jeffrey M. Spraggins − *Department of Chemistry, Mass Spectrometry Research Center, and Department of Biochemistry, Vanderbilt University, Nashville, Tennessee 37235, United States;* orcid.org/0000-0001-9198-5498; Email: Jeff.Spraggins@vanderbilt.edu

Authors

Katerina V. Djambazova − *Department of Chemistry and Mass Spectrometry Research Center, Vanderbilt University, Nashville, Tennessee 37235, United States*

Dustin R. Klein − *Mass Spectrometry Research Center and Department of Biochemistry, Vanderbilt University, Nashville, Tennessee 37235, United States*

Lukasz G. Migas − *Delft Center for Systems and Control, Delft University of Technology, 2628 CD Delft, The Netherlands;* orcid.org/0000-0002-1884-6405

Elizabeth K. Neumann − *Mass Spectrometry Research Center and Department of Biochemistry, Vanderbilt University, Nashville, Tennessee 37235, United States;* orcid.org/0000-0002-6078-3321

Emilio S. Rivera − *Mass Spectrometry Research Center and Department of Biochemistry, Vanderbilt University, Nashville, Tennessee 37235, United States*

Raf Van de Plas − *Delft Center for Systems and Control, Delft University of Technology, 2628 CD Delft, The Netherlands;* orcid.org/0000-0002-2232-7130

Richard M. Caprioli − *Department of Chemistry, Mass Spectrometry Research Center, Department of Biochemistry, Department of Pharmacology, and Department of Medicine, Vanderbilt University, Nashville, Tennessee 37235, United States*

Complete contact information is available at: https://pubs.acs.org/10.1021/acs.analchem.0c02520

Author Contributions

All authors have given approval to the final version of the manuscript.

Notes

The authors declare no competing financial interest.

■ ACKNOWLEDGMENTS

Support was provided by The National Science Foundation Major Research Instrument Program (CBET—1828299 awarded to J.M.S. and R.M.C.) and The National Institutes of Health (NIH) National Institute of General Medical Sciences (P41 GM103391 awarded to R.M.C.). The 15T FT-ICR MS in the Mass Spectrometry Research Center at Vanderbilt University was acquired through the NIH Shared Instrumentation Grant Program (1S10OD012359). E.K.N. is supported by a National Institute of Environmental Health Sciences training grant (T32ES007028). The authors wish to thank Terry Dermody from the University of Pittsburgh for providing the mouse pup and Daniel Ryan for sample assistance.

■ REFERENCES

(1) Shevchenko, A.; Simons, K. *Nat. Rev. Mol. Cell. Biol.* **2010**, *11*, 593−598.
(2) Liebisch, G.; Vizcaíno, J. A.; Köfeler, H.; Trötzmüller, M.; Griffiths, W. J.; Schmitz, G.; Spener, F.; Wakelam, M. J. O. *J. Lipid Res.* **2013**, *54*, 1523−1530.
(3) Yang, K.; Han, X. *Trends Biochem. Sci.* **2016**, *41*, 954−969.
(4) O'Donnell, V. B.; Ekroos, K.; Liebisch, G.; Wakelam, M. *Wiley Interdiscip. Rev.: Syst. Biol. Med.* **2020**, *12*, No. e1466.
(5) Rustam, Y. H.; Reid, G. E. *Anal. Chem.* **2018**, *90*, 374−397.
(6) Caprioli, R. M.; Farmer, T. B.; Gile, J. *Anal. Chem.* **1997**, *69*, 4751−4760.
(7) Angel, P. M.; Spraggins, J. M.; Baldwin, H. S.; Caprioli, R. *Anal. Chem.* **2012**, *84*, 1557−1564.
(8) Zemski Berry, K. A.; Hankin, J. A.; Barkley, R. M.; Spraggins, J. M.; Caprioli, R. M.; Murphy, R. C. *Chem. Rev.* **2011**, *111*, 6491.
(9) Cohen, L. H.; Gusev, A. I. *Anal. Bioanal. Chem.* **2002**, *373*, 571−586.
(10) Bhandari, D. R.; Schott, M.; Römpp, A.; Vilcinskas, A.; Spengler, B. *Anal. Bioanal. Chem.* **2015**, *407*, 2189−2201.
(11) Powers, T. W.; Neely, B. A.; Shao, Y.; Tang, H.; Troyer, D. A.; Mehta, A. S.; Haab, B. B.; Drake, R. R. *PLoS One* **2014**, *9*, No. e106255.
(12) Drake, R. R.; Powers, T. W.; Norris-Caneda, K.; Mehta, A. S.; Angel, P. M. *Curr. Protoc. Protein Sci.* **2018**, *94*, No. e68.
(13) Schober, Y.; Guenther, S.; Spengler, B.; Römpp, A. *Rapid Commun. Mass Spectrom.* **2012**, *26*, 1141−1146.
(14) Prentice, B. M.; Ryan, D. J.; Van De Plas, R.; Caprioli, R. M.; Spraggins, J. M. *Anal. Chem.* **2018**, *90*, 5090−5099.
(15) Spraggins, J. M.; Caprioli, R. M. *J. Am. Soc. Mass Spectrom.* **2011**, *22*, 1022−1031.
(16) El-Aneed, A.; Cohen, A.; Banoub, J. *Appl. Spectrosc. Rev.* **2009**, *44*, 210−230.
(17) Smith, D. F.; Kiss, A.; Leach, F. E.; Robinson, E. W.; Paša-Tolić, L.; Heeren, R. M. A. *Anal. Bioanal. Chem.* **2013**, *405*, 6069−6076.
(18) Kompauer, M.; Heiles, S.; Spengler, B. *Nat. Methods* **2017**, *14*, 90−96.
(19) Murphy, R. C.; Hankin, J. A.; Barkley, R. M. *J. Lipid Res.* **2009**, *50*, S317−S322.
(20) Tang, F.; Guo, C.; Ma, X.; Zhang, J.; Su, Y.; Tian, R.; Shi, R.; Xia, Y.; Wang, X.; Ouyang, Z. *Anal. Chem.* **2018**, *90*, 5612−5619.
(21) Kozlowski, R. L.; Mitchell, T. W.; Blanksby, S. J. *Sci. Rep.* **2015**, *5*, No. 9243.

(22) Klein, D. R.; Feider, C. L.; Garza, K. Y.; Lin, J. Q.; Eberlin, L. S.; Brodbelt, J. S. *Anal. Chem.* **2018**, *90*, 10100−10104.
(23) Porta Siegel, T.; Ekroos, K.; Ellis, S. R. *Angew. Chem., Int. Ed.* **2019**, *58*, 6492−6501.
(24) Damen, C. W. N.; Isaac, G.; Langridge, J.; Hankemeier, T.; Vreeken, R. J. *J. Lipid Res.* **2014**, *55*, 1772−1783.
(25) Lamont, L.; Baumert, M.; Ogrinc Potočnik, N.; Allen, M.; Vreeken, R.; Heeren, R. M. A.; Porta, T. *Anal. Chem.* **2017**, *89*, 11143−11150.
(26) May, J. C.; Goodwin, C. R.; Lareau, N. M.; Leaptrot, K. L.; Morris, C. B.; Kurulugama, R. T.; Mordehai, A.; Klein, C.; Barry, W.; Darland, E.; et al. *Anal. Chem.* **2014**, *86*, 2107−2116.
(27) Valentine, S. J.; Koeniger, S. L.; Clemmer, D. E. *Anal. Chem.* **2003**, *75*, 6202−6208.
(28) Zhong, Y.; Hyung, S.-J.; Ruotolo, B. T. *Analyst* **2011**, *136*, 3534.
(29) Shvartsburg, A. A.; Smith, R. D. *Anal. Chem.* **2008**, *80*, 9689−9699.
(30) Purves, R. W.; Guevremont, R. *Anal. Chem.* **1970**, *52*, 2346−2357.
(31) Kolakowski, B. M.; Mester, Z. *Analyst* **2007**, *132*, 842.
(32) Guevremont, R. *J. Chromatogr. A* **2004**, *1058*, 3−19.
(33) Fernandez-Lima, F.; Kaplan, D. A.; Suetering, J.; Park, M. A. *Int. J. Ion Mobility Spectrom.* **2011**, *14*, 93−98.
(34) Michelmann, K.; Silveira, J. A.; Ridgeway, M. E.; Park, M. A. *J. Am. Soc. Mass Spectrom.* **2015**, *26*, 14−24.
(35) Groessl, M.; Graf, S.; Knochenmuss, R. *Analyst* **2015**, *140*, 6904−6911.
(36) Zheng, X.; Smith, R. D.; Baker, E. S. *Curr. Opin. Chem. Biol* **2018**, *42*, 111−118.
(37) Kyle, J. E.; Zhang, X.; Weitz, K. K.; Monroe, M. E.; Ibrahim, Y. M.; Moore, R. J.; Cha, J.; Sun, X.; Lovelace, E. S.; Wagoner, J.; et al. *Analyst* **2016**, *141*, 1649−1659.
(38) McLean, J. A.; Ridenour, W. B.; Caprioli, R. M. *J. Mass Spectrom.* **2007**, *42*, 1099−1105.
(39) Škrášková, K.; Claude, E.; Jones, E. A.; Towers, M.; Ellis, S. R.; Heeren, R. M. A. *Methods* **2016**, *104*, 69−78.
(40) Deng, L.; Ibrahim, Y. M.; Baker, E. S.; Aly, N. A.; Hamid, A. M.; Zhang, X.; Zheng, X.; Garimella, S. V. B.; Webb, I. K.; Prost, S. A.; et al. *ChemistrySelect* **2016**, *1*, 2396−2399.
(41) Ibrahim, Y. M.; Hamid, A. M.; Deng, L.; Garimella, S. V. B.; Webb, I. K.; Baker, E. S.; Smith, R. D. *Analyst* **2017**, *142*, 1010−1021.
(42) Wojcik, R.; Webb, I. K.; Deng, L.; Garimella, S. V. B.; Prost, S. A.; Ibrahim, Y. M.; Baker, E. S.; Smith, R. D. *Int. J. Mol. Sci.* **2017**, *18*, 183.
(43) Tolmachev, A. V.; Webb, I. K.; Ibrahim, Y. M.; Garimella, S. V.B.; Zhang, X.; Anderson, G. A.; Smith, R. D. *Anal. Chem.* **2014**, *86* (18), 9162−9168.
(44) Bowman, A. P.; Abzalimov, R. R.; Shvartsburg, A. A. *J. Am. Soc. Mass Spectrom.* **2017**, *28*, 1552−1561.
(45) Nagy, G.; Veličković, D.; Chu, R. K.; Carrell, A. A.; Weston, D. J.; Ibrahim, Y. M.; Anderton, C. R.; Smith, R. D. *Chem. Commun.* **2019**, *55*, 306−309.
(46) Sans, M.; Feider, C. L.; Eberlin, L. S. *Curr. Opin. Chem. Biol.* **2018**, *42*, 138−146.
(47) Shvartsburg, A. A.; Isaac, G.; Leveque, N.; Smith, R. D.; Metz, T. O. *J. Am. Soc. Mass Spectrom.* **2011**, *22*, 1146−1155.
(48) Lintonen, T. P.; Baker, P. R. S.; Suoniemi, M.; Ubhi, B. K.; Koistinen, K. M.; Duchoslav, E.; Campbell, J. L.; Ekroos, K. *Anal. Chem.* **2014**, *86*, 9662−9669.
(49) Feider, C. L.; Elizondo, N.; Eberlin, L. S. *Anal. Chem.* **2016**, *88*, 11533−11541.
(50) Spraggins, J. M.; Djambazova, K. V.; Rivera, E. S.; Migas, L. G.; Neumann, E. K.; Fuetterer, A.; Suetering, J.; Goedecke, N.; Ly, A.; Van De Plas, R.; et al. *Anal. Chem.* **2019**, *91*, 14552−14560.
(51) Ridgeway, M. E.; Lubeck, M.; Jordens, J.; Mann, M.; Park, M. A. *Int. J. Mass Spectrom.* **2018**, *425*, 22−35.
(52) Hernandez, D. R.; DeBord, J. D.; Ridgeway, M. E.; Kaplan, D. A.; Park, M. A.; Fernandez-Lima, F. *Analyst* **2014**, *139*, 1913−1921.
(53) Silveira, J. A.; Ridgeway, M. E.; Park, M. A. *Anal. Chem.* **2014**, *86*, 5624−5627.
(54) Jeanne Dit Fouque, K.; Ramirez, C. E.; Lewis, R. L.; Koelmel, J. P.; Garrett, T. J.; Yost, R. A.; Fernandez-Lima, F. *Anal. Chem.* **2019**, *91*, 5021−5027.
(55) Fu, T.; Oetjen, J.; Chapelle, M.; Verdu, A.; Szesny, M.; Chaumot, A.; Degli-Esposti, D.; Geffard, O.; Clément, Y.; Salvador, A.; et al. *J. Mass Spectrom.* **2020**, *55*, No. e4531.
(56) Fahy, E.; Sud, M.; Cotter, D.; Subramaniam, S. *Nucleic Acids Res.* **2007**, *35*, W606−W612.
(57) Fahy, E.; Subramaniam, S.; Murphy, R. C.; Nishijima, M.; Raetz, C. R. H.; Shimizu, T.; Spener, F.; Van Meer, G.; Wakelam, M. J. O.; Dennis, E. A. *J. Lipid Res.* **2009**, *50*, S9−S14.
(58) Bielow, C.; Mastrobuoni, G.; Orioli, M.; Kempa, S. *Anal. Chem.* **2017**, *89*, 2986−2994.
(59) Wang, M.; Huang, Y.; Han, X. *Rapid Commun. Mass Spectrom.* **2014**, *28*, 2201−2210.
(60) Jeanne Dit Fouque, K.; Ramirez, C. E.; Lewis, R. L.; Koelmel, J. P.; Garrett, T. J.; Yost, R. A.; Fernandez-Lima, F. *Anal. Chem.* **2019**, *91*, 5021−5027.
(61) Hankin, J. A.; Murphy, R. C.; Barkley, R. M.; Gijón, M. A. *Int. J. Mass Spectrom.* **2015**, *378*, 255−263.
(62) Anderson, D. M. G.; Ablonczy, Z.; Koutalos, Y.; Hanneken, A. M.; Spraggins, J. M.; Calcutt, M. W.; Crouch, R. K.; Caprioli, R. M.; Schey, K. L. *Sci. Rep.* **2017**, *7*, No. 17352.
(63) Akgoc, Z.; Sena-Esteves, M.; Martin, D. R.; Han, X.; D'Azzo, A.; Seyfried, T. N. *J. Lipid Res.* **2015**, *56*, 1006−1013.
(64) Numata, M.; Chu, H. W.; Dakhama, A.; Voelker, D. R. *Proc. Natl. Acad. Sci. U.S.A.* **2010**, *107*, 320−325.
(65) Janmey, P. A.; Kinnunen, P. K. J. *Trends Cell. Biol.* **2006**, *16*, 538−546.
(66) Sandra, K.; Sandra, P. *Curr. Opin. Chem. Biol.* **2013**, *17*, 847−853.
(67) Lewis, B. A.; Engelman, D. M. *J. Mol. Biol.* **1983**, *166*, 211−217.
(68) Mitchell, T. W.; Pham, H.; Thomas, M. C.; Blanksby, S. J. *J. Chromatogr. B* **2009**, *877*, 2722−2735.
(69) Brown, S. H. J.; Mitchell, T. W.; Oakley, A. J.; Pham, H. T.; Blanksby, S. J. *J. Am. Soc. Mass Spectrom.* **2012**, *23*, 1441−1449.
(70) Paine, M. R. L.; Poad, B. L. J.; Eijkel, G. B.; Marshall, D. L.; Blanksby, S. J.; Heeren, R. M. A.; Ellis, S. R. *Angew. Chem., Int. Ed.* **2018**, *57*, 10530−10534.

https://dx.doi.org/10.1021/acs.analchem.0c02520
Anal. Chem. 2020, 92, 13290−13297